INTERFACE

royalsocietypublishing.org/journal/rsif

Research

Cite this article: Lipková J, Menze B, Wiestler B, Koumoutsakos P, Lowengrub JS. 2022 Modelling glioma progression, mass effect and intracranial pressure in patient anatomy. *J. R. Soc. Interface* **19**: 20210922. https://doi.org/10.1098/rsif.2021.0922

Received: 10 December 2021
Accepted: 21 February 2022

Subject Category:
Life Sciences–Mathematics interface

Subject Areas:
biomathematics, computational biology, medical physics

Keywords:
glioma, patient-specific modelling, tumour mass effect, brain deformation, intracranial pressure

Authors for correspondence:
Jana Lipková
e-mail: jlipkova@bwh.harvard.edu
John S. Lowengrub
e-mail: jlowengr@uci.edu

THE ROYAL SOCIETY PUBLISHING

Modelling glioma progression, mass effect and intracranial pressure in patient anatomy

Jana Lipková[1,2,3], Bjoern Menze[4,5,6], Benedikt Wiestler[6], Petros Koumoutsakos[7,8] and John S. Lowengrub[9,10,11]

[1]Department of Pathology, Brigham and Women's Hospital, Harvard Medical School, Boston, MA, USA
[2]Dana-Farber Cancer Institute, Boston, MA, USA
[3]Broad Institute of Harvard and MIT, Cambridge, MA, USA
[4]Department of Informatics, Technical University of Munich, Munich, Germany
[5]Department of Quantitative Biomedicine, University of Zürich, Zürich, Switzerland
[6]Department of Neuroradiology, Klinikum Rechts der Isar, Technical University of Munich, Munich, Germany
[7]Computational Science and Engineering Lab, ETH Zürich, Zürich, Switzerland
[8]School of Engineering and Applied Sciences, Harvard University, Cambridge, MA 02138, USA
[9]Department of Mathematics, University of California, Irvine, CA, USA
[10]Department of Biomedical Engineering, University of California, Irvine, CA, USA
[11]Center for Complex Biological Systems, Chao Family Comprehensive Cancer Center, University of California, Irvine, CA, USA

JL, 0000-0001-8101-4794; BM, 0000-0003-4136-5690; BW, 0000-0002-2963-7772; PK, 0000-0001-8337-2122; JSL, 0000-0003-1759-0900

Increased intracranial pressure is the source of most critical symptoms in patients with glioma, and often the main cause of death. Clinical interventions could benefit from non-invasive estimates of the pressure distribution in the patient's parenchyma provided by computational models. However, existing glioma models do not simulate the pressure distribution and they rely on a large number of model parameters, which complicates their calibration from available patient data. Here we present a novel model for glioma growth, pressure distribution and corresponding brain deformation. The distinct feature of our approach is that the pressure is directly derived from tumour dynamics and patient-specific anatomy, providing non-invasive insights into the patient's state. The model predictions allow estimation of critical conditions such as intracranial hypertension, brain midline shift or neurological and cognitive impairments. A diffuse-domain formalism is employed to allow for efficient numerical implementation of the model in the patient-specific brain anatomy. The model is tested on synthetic and clinical cases. To facilitate clinical deployment, a high-performance computing implementation of the model has been publicly released.

1. Introduction

Glioma is the most common type of primary brain tumour. Gliomas are divided into low- and high-grade tumours. High-grade gliomas (HGGs) are characterized by fast progression and poor prognosis with a median survival between 1 and 5 years, depending on the tumour subtype [1–3]. Low-grade gliomas (LGGs) progress at a slower pace and have a better prognosis; however, most LGGs eventually progress to HGGs [4]. In contrast to other primary malignancies, glioma manifests not only as an oncological but also as a neurological disease. The most common symptoms include: drowsiness (87%), progressive neurological (51%) and cognitive (33%) deficits, seizures (45%), incontinence (40%) and headaches (33%) [5–7]. The majority of the symptoms stem from increased intracranial pressure (ICP), which is also the main cause of death [8,9]. The corresponding mechanical forces further affect the tumour micro-

environment and treatment efficacy [10]. The standard-of-care treatment of gliomas follows the Stupp protocol [1], which consists of combined surgery and chemo- and radiotherapy. Despite extensive efforts, gliomas are still incurable. Tumour management is complicated not only by the delicate nature of the brain tissue but also by the infiltrative growth of gliomas. In contrast to most cancers, gliomas do not form solid tumours with well-defined boundaries; instead, they infiltrate surrounding brain tissue even beyond the tumour borders visible on medical scans. The inability of current imaging methods to detect the whole tumour extent and pressure distribution contribute to the overall treatment complexity.

Computational tumour models can provide valuable insights into the patient's state and forecast the disease progression to assist clinical interventions. Most glioma models are based on the Fisher–Kolmogorov equation, which describes tumour proliferation and infiltration into the surrounding tissue [11–24]. Such models have been used to simulate spatio-temporal disease progression, response to treatment or transition from LGGs to HGGs [14,23,25–30]. The models can be further calibrated to patient-specific conditions to provide estimates about tumour infiltration pathways beyond the lesion outlines visible on medical scans [17,24,31–38]. Such estimates were, for instance, used to design personalized radiotherapy plans to spare healthy tissue and reduce radiation toxicity [31] or to predict response to treatment [35]. However, since these models do not account for the mechanical interactions between the growing tumour and surrounding brain tissue—the so-called tumour mass effect—their validity is limited to a short time scale before the tumour mass effect becomes significant. The clinical potential of glioma models can thus be significantly increased by accounting for the tumour mass effect and tumour-induced pressure in the patient's brain.

Although there is great interest in modelling brain biomechanical processes and deformations, not all existing models are suitable for glioma progression. For instance, a large body of models focus on modelling intraoperative brain deformations [39–43] or changes caused by traumatic brain injuries [44–46]. These models, however, consider biomechanical deformations caused by short-term forces acting from outside the skull, such as surgical loads, craniotomy-induced brain shift or impact head injury. Early models describing tumour-induced brain deformations originate from works by Mohamed *et al.* [47] and Hogea *et al.* [48], where brain tissue is modelled as an elastic material and tumour mechanical forces are approximated by a constant pressure acting on the tumour boundary. These models were designed for the construction of statistical brain atlases bearing tumours, and thus they do not account for tumour proliferation or infiltration. This issue was overcome by Clatz *et al.* [49], who combined the mechanical model with the Fisher–Kolmogorov equation describing tumour progression. The model was further updated by Abler *et al.* [50], who included additional linear coupling between tumour cell density and the growth-induced strain. In these models [49,50], however, the tumour dynamics is decoupled from the tissue deformation equation, which can lead to discrepancies, especially in the case of large deformations. A further improvement came from work by Hogea *at al.* [51,52], who used a nonlinear reaction–advection–diffusion equation to couple the tumour growth with brain tissue deformation, enabling simulations of large brain deformations. The model has been used in several simulation studies as well as medical image-processing tasks [33,53–56]. Recently, the model has been extended to account for different tumour components, such as proliferating, invasive and necrotic tumour cells, along with tumour-induced brain oedema, resulting in realistically appearing simulated tumours [57].

Despite considerable theoretical contributions, these models suffer from two main limitations. First, none of the previous models simulates the pressure distribution in the patient's brain. The existing models either do not consider the pressure term at all or the pressure is modelled as a constant increment, uniform in the whole brain, regardless of the tumour size or location. As a consequence, these models cannot provide any estimates of the pressure distribution or pressure-related symptoms, such as intracranial hypertension. Second, the models rely on a large number of parameters, which complicates their calibration to patient-specific conditions. Many parameters can be rendered patient- or disease-specific; however, inferring their values from the limited amount of non-invasive patient data is a challenging task. For instance, although medical scans reveal compression of brain tissues, this information might not be sufficient to identify the mechanical properties of individual tissue constituents as described by Young's modulus, Poisson's ratio and other model parameters. Computational simulations thus usually rely on parameter values obtained from *in vivo* animal experiments or post-mortem studies. However, several studies have demonstrated large intra-species variations as well as rapid changes in brain tissue properties even a few minutes after death [58]. This in turn leads to a large variation in parameter values used across the literature [47,49,51], which further affects the ability of the computational models to provide patient-specific predictions.

To address these limitations, herein, we propose a novel glioma model that couples tumour dynamics, brain tissue deformation and corresponding ICP changes in the patient-specific anatomy. The model assumes that the growing tumour exerts pressure on the surrounding brain tissue, which is treated as a viscoelastic material. The brain tissues partially relax the pressure, depending on the tissue-specific properties, while the remaining pressure results in the deformation force. ICP is directly derived from the growing tumour, and it is constrained by patient-specific anatomy, enabling estimation of the pressure distribution in the whole patient parenchyma. The model predictions can be used to assess neurological and cognitive impairments caused by increased pressure in the patient-specific brain centres as well as predict onset of critical conditions such as intracranial hypertension (table 1) or brain midline shift [9,69]—a condition in which the brain moves towards one side of parenchyma, where a displacement above 5 mm usually requires immediate surgical intervention [70,71]. The estimated ICP distribution can help identify the regions with the highest pressure accumulation, which holds the potential to assist surgical interventions aiming to release the ICP.

To facilitate model calibration for patient-specific predictions, the model uses a small number of parameters, as listed in table 2. Alongside the proposed model we present an efficient numerical formulation to facilitate the model implementation. The model is solved directly in the patient's medical scans using the finite-difference (FD) method. In comparison, previous works used mainly finite-element methods since the FD approach often results in a large system of

Table 1. Relations between ICP values and corresponding pathological conditions [59–64]. While there are rare cases [65,66] with survival reported in patients with ICP >50 (mmHg), increased ICP is consistently associated with high mortality [62,67,68].

ICP (mmHg)	ICP (Pa)	condition
7–15	933–1999	normal
20–25	2666–3333	onset of hypertension
25–40	3333–5332	hypertension
40–50	5332–6666	loss of consciousness
>50	>6666	brain infraction and brain death

Table 2. An overview of the model parameters and their units. The parameters T (day), L (cm) and M (g) denote the characteristic time, length and mass, respectively. The growing tumour $\boldsymbol{u}$ proliferates at rate ρ and infiltrates the surrounding brain tissue with tissue-specific infiltration rate $\mathbb{D}$. As the tumour grows it exerts pressure $\boldsymbol{p}$ on the surrounding brain tissue. The hydraulic conductivity $\mathcal{M}$ describes the ease with which the pressure passes through the brain tissues. Individual brain tissues partially relax the pressure, depending on the tissue-specific relaxation properties given by $\boldsymbol{\kappa}$, while the resulting pressure leads to tissue translation and compression described by the deformation rate $\vec{\boldsymbol{v}}$.

variable	units	description
$\boldsymbol{u}$	M/L^3	tumour cell density
$\boldsymbol{\omega}$	M/L^3	brain tissue cell density
$\mathbb{D}$	L^2/T	tumour infiltration rate
ρ	$1/T$	tumour proliferation rate
$\boldsymbol{p}$	M/LT^2	tumour-induced pressure
$\boldsymbol{\kappa}$	T/L^2	pressure relaxation
$\vec{\boldsymbol{v}}$	L/T	deformation rate
$\mathcal{M}$	L^3/TM	hydraulic conductivity

linear equations with a non-symmetric matrix, which complicates the numerical implementation [51]. The symmetry of the system is broken by the boundary conditions applied to the complex brain anatomy. To overcome this issue, we deploy the diffuse domain method (DDM) [72], which significantly reduces the numerical and computational complexity of the system. To further ease the model deployment, a high-performance model implementation is publicly released.[1]

The rest of the paper is structured as follows: the proposed model is introduced in §2, followed by a description of the numerical implementation and the DDM formalism. The results are presented in §3, where the model is applied to synthetic and clinical cases. The relationship between ICP elevation and neurological symptoms is explored. The conclusion is presented in §4.

2. Methods

2.1. Biomechanical model

This section describes the proposed biomechanical model for glioma progression, mass effect and ICP dynamics in the patient-specific brain anatomy. The physics of the underlying process can be summarized as follows. The tumour proliferates and infiltrates the surrounding brain tissue, which consists of white matter, grey matter and cerebrospinal fluid (CSF). The brain tissue is assumed to consist of viscoelastic materials, where distinct tissue constituents are characterized by different mechanical properties. The growing tumour exerts pressure on the surrounding brain tissue. The pressure is partially relaxed by the brain tissue, depending on the tissue-specific mechanical properties, while the remaining pressure results in tissue deformation and compression. This mechanism entails three coupled processes: (i) tumour dynamics, (ii) pressure dynamics, and (iii) tissue dynamics; these represent the three main components of the model described in the following subsections.

To facilitate the model description, the rest of this paragraph outlines the notation and assumptions. The model is solved in the patient-specific brain anatomy reconstructed from magnetic resonance imaging (MRI) scans, where each image voxel corresponds to one simulation grid point. The letter $i \in \{1, \ldots, N\}$ denotes an index across all N voxels of the MRI scan. It is assumed that the tumour cells infiltrate only white and grey matter, whereas the pressure affects all the tissues in the brain parenchyma. According to this assumption, we consider three distinct simulation domains: $\Omega_1(t) \in \mathbb{R}^3$, a domain consisting of white and grey matter only; $\Omega_2 \in \mathbb{R}^3$, a domain including white matter, grey matter and CSF (i.e. the whole brain parenchyma); $\Omega_3 \in \mathbb{R}^3$, a regular domain containing the brain parenchyma and skull (e.g. whole brain scan). Figure 1 shows the three simulation domains, and it is assumed that $\Omega_1(t) \subset \Omega_2 \subset \Omega_3$. We note that the border of the domain $\Omega_1(t)$ changes over time t as a result of the tumour-induced changes, such as tissue displacement. On the other hand, the borders of the domains Ω_2 and Ω_3 are constant over time, since Ω_2 is constrained by a rigid skull and Ω_3 is defined as a fixed domain. To distinguish the different scopes of model variables, the following labelling is used: the field variables defined at every voxel, such as tumour cell density, are marked by bold letters, e.g. $\boldsymbol{x}$; the vectors of field variables, such as deformation rate, are denoted by bold letters with an arrow, e.g. $\vec{\boldsymbol{x}}$; scalar variables, such as the proliferation rate, are marked by non-bold letters, e.g. x. An overview of the model parameters is provided in table 2.

2.1.1. Tumour dynamics

The glioma dynamic consists of tumour proliferation and infiltration into the surrounding brain tissue. Let $u_i(t) \in [0, 1]$ be a normalized tumour cell density at time t and voxel $i \in \{1, \ldots, N\}$ at location $(i_x, i_y, i_z) \in \Omega_1(t)$. The dynamics of the tumour cell density $\boldsymbol{u} := \{u_i(t)\}_{i=1}^N$ in the brain tissue $\Omega_1(t)$ is modelled as:

$$\frac{\partial \boldsymbol{u}}{\partial t} = \nabla \cdot (\mathbb{D} \nabla \boldsymbol{u}) + \rho \boldsymbol{u}(\mathbf{1} - \boldsymbol{u}) - \vec{\boldsymbol{v}} \cdot \nabla \boldsymbol{u} \quad \text{in } \Omega_1(t), \tag{2.1}$$

$$\nabla \boldsymbol{u} \cdot \vec{\boldsymbol{n}} = \mathbf{0} \quad \text{in } \partial\Omega_1(t), \tag{2.2}$$

$$\boldsymbol{u}(\boldsymbol{t} = \mathbf{0}) = \boldsymbol{u_0} \quad \text{in } \Omega_1(t = \mathbf{0}). \tag{2.3}$$

The first term on the right-hand side of equation (2.1) describes tumour infiltration into the surrounding brain tissue, where $\mathbb{D} = \{D_i(t)\,\mathbb{I}\}_{i=1}^N$ is a tissue-dependent tensor, $\mathbb{I}$ is a 3×3 identity matrix and

$$D_i(t) = \begin{cases} p_{w_i}(t)\, D_w + p_{g_i}(t)\, D_g & \text{for } i \in \Omega_1(t), \\ 0 & \text{for } i \notin \Omega_1(t), \end{cases} \tag{2.4}$$

where $p_{w_i}(t)$ and $p_{g_i}(t)$ denote the percentage of the white and grey matter at voxel i at time t. The constants D_w and D_g describe the tumour infiltration rate in white and grey matter, respectively. Since the tumour cells infiltrate the white matter faster than the grey matter, it is assumed that $D_w = 10 D_g\ (\mathrm{cm}^2\,\mathrm{day}^{-1})$ [24,73]. Let us note that the tissue

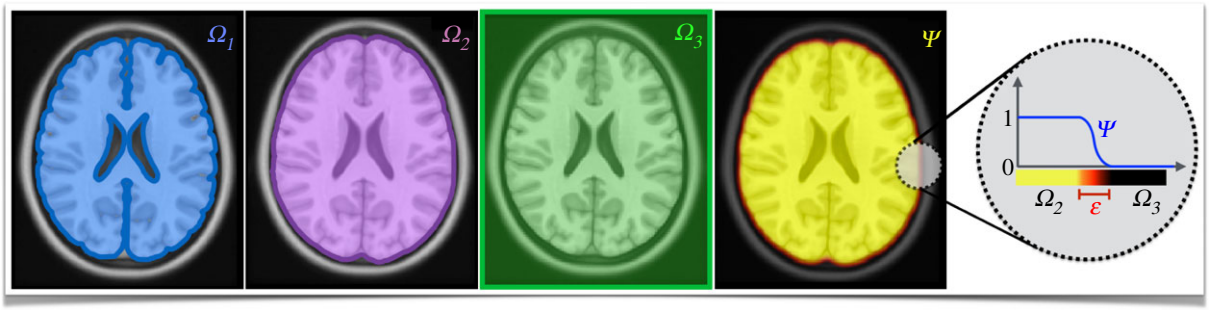

Figure 1. An overview of the simulation domains and the phase-field function. Three distinct simulation domains $\Omega_1 \subset \Omega_2 \subset \Omega_3 \in \mathbb{R}^3$ are considered to capture different processes. It is assumed that the tumour infiltrates only white and grey matter, which together constitute the domain Ω_1 shown in blue. The tumour mass effect and pressure affect the whole-brain parenchyma; this is captured by domain Ω_2, displayed in purple. A regular domain used for DDM formulation, Ω_3, is portrayed in green. The last subplot shows the phase-field function ψ used to capture the relation between domains Ω_2 and Ω_3.

percentages $p_{w_i}(t)$ and $p_{g_i}(t)$ change over time owing to the tumour-induced tissue displacement. The second term on the right-hand side of equation (2.1) describes self-limiting tumour proliferation, where ρ (1/day) is the proliferation rate. As the tumour grows, it exerts pressure on the surrounding tissue, which is deformed and displaced in response. The brain tissue displacement also causes displacement of the tumour cells infiltrated inside that tissue. This is modelled by the last term on the right-hand side of equation (2.1), where $\vec{v} := \{(v_{x_i}(t), v_{y_i}(t), v_{z_i}(t))\}_{i=1}^N$ is the rate of displacement. The skull and CSF (including ventricles) are not infiltrated by the tumour and act as a domain boundary with an imposed no-flux boundary condition given by equation (2.2), where $\vec{n}$ is the unit outward normal to $\partial\Omega_1(t)$. The tumour is initialized as a point source at voxel $i_{ic} \in \Omega_1(t=0)$ and its growth is modelled from the initial time $t=0$ until the final time $t=T$ (day).

2.1.2. Pressure dynamics

The pressure dynamics are determined by the growing tumour pressing on the surrounding brain tissue and the mechanical properties of the individual tissue constituents. The brain tissue acts as a viscoelastic material that partially relaxes the pressure from the tumour. The pressure relaxation is proportional to the tissue-specific mechanical properties—the softer the material the more pressure it relaxes. The remaining pressure results in tissue deformation. The deformation rate can be computed from the pressure gradient using Darcy's law. Let $\vec{v}$ denote the deformation rate. For the pressure term, we will assume that $\boldsymbol{p}(\boldsymbol{t}=\boldsymbol{0})$ is the patient's normal pressure before the onset of the tumour and $\boldsymbol{p}'(\boldsymbol{t})$ is the patient's pressure with the tumour at time t. The tumour-induced pressure $\boldsymbol{p}(\boldsymbol{t})$ is then given as $\boldsymbol{p}(\boldsymbol{t}) = \boldsymbol{p}'(\boldsymbol{t}) - \boldsymbol{p}(\boldsymbol{t}=\boldsymbol{0})$. Since the exact values of the patient's normal pressure are not known, we will assume $\boldsymbol{p}(\boldsymbol{t}=\boldsymbol{0}) = \boldsymbol{0}$ and use the following equations to simulate the dynamics of the tumour-induced pressure $\boldsymbol{p}(\boldsymbol{t})$ in the domain Ω_2:

$$\vec{v} = -\mathcal{M} \cdot \nabla p \quad \text{in } \Omega_2, \tag{2.5}$$

$$\nabla \cdot \vec{v} = \rho u(1-u) - \varkappa p \quad \text{in } \Omega_2, \tag{2.6}$$

$$\vec{v} = 0 \quad \text{on } \partial\Omega_2. \tag{2.7}$$

The parameter $\mathcal{M}$, sometimes referred to as hydraulic conductivity, describes the ease with which the pressure passes through the tissue. The pressure relaxation is described by the parameter $\boldsymbol{\varkappa} := \{\varkappa_i(t)\}_{i=1}^N$, where

$$\varkappa_i(t) = \begin{cases} p_{w_i}(t)\,\varkappa_w + p_{g_i}(t)\,\varkappa_g + p_{c_i}(t)\,\varkappa_c & \text{for } i \in \Omega_2, \\ 0 & \text{for } i \notin \Omega_2. \end{cases} \tag{2.8}$$

The terms $p_{w_i}(t)$, $p_{g_i}(t)$, $p_{c_i}(t)$ denote the percentage of white matter, grey matter and CSF at voxel i at time t, while $\varkappa_w$, $\varkappa_g$ and $\varkappa_c$ denote the relaxation rate of the corresponding tissues. The softer the material is, the more pressure it relaxes; thus, it is assumed that $\varkappa_c > \varkappa_w > \varkappa_g$. For simplicity, we assume constant hydraulic conductivity $\mathcal{M} = 8.53 \times 10^{-9}\,(\mathrm{cm}^2 \cdot \mathrm{mmHg}^{-1} \cdot \mathrm{s}^{-1})$, as reported in [74]. This means that the tumour exerts the same pressure on all surrounding tissues, but distinct tissues respond differently depending on their mechanical properties. By substituting equation (2.5) into both equations (2.6) and (2.7) we obtain a Helmholtz-like equation, which allows the computation of the pressure field as

$$-\nabla \cdot (\mathcal{M} \cdot \nabla p) = \rho u(1-u) - \varkappa p \quad \text{in } \Omega_2, \tag{2.9}$$

$$\nabla p \cdot \vec{n} = 0 \quad \text{on } \partial\Omega_2. \tag{2.10}$$

The pressure $\boldsymbol{p}$ obtained by solving equations (2.9) and (2.10) is used to compute the deformation rate $\vec{v}$ from (2.5), which is consequently used to model the tissue deformation.

2.1.3. Tissue dynamics

The growing tumour compresses and displaces the surrounding brain tissue. Let $\omega_{w_i}(t)$, $\omega_{g_i}(t)$ and $\omega_{c_i}(t)$ denote the cell density of white matter, grey matter and CSF, respectively, at voxel $i \in \Omega_2$ at time t. The dynamics of each tissue constituent $\boldsymbol{\omega}_s := \{\omega_{s_i}(t)\}_{i=1}^N$, $s \in \{w, g, c\}$ is modelled by the following advection–convection equation:

$$\frac{\partial \omega_s}{\partial t} = -\vec{v} \cdot \nabla \omega_s - \omega_s \nabla \cdot \vec{v} \quad \text{in } \Omega_2, \tag{2.11}$$

$$\nabla \omega_s \cdot \vec{n} = 0 \quad \text{on } \partial\Omega_2, \tag{2.12}$$

$$\omega_s(t=0) = \omega_{s_0} \quad \text{in } \Omega_2. \tag{2.13}$$

The cell density of each tissue component in equation (2.13) is initialized from the tissue segmentation, which can be computed with the provided open-source software.[2] The advection term describes tissue displacement, while the convection term models tissue compression. After each simulation time step, the percentage of each tissue component must be recomputed accordingly, i.e. for $\forall i \in \Omega_2$ and $s \in \{w, g, c\}$

$$p_{s_i}(t) = \frac{\omega_{s_i}(t)}{\omega_{w_i}(t) + \omega_{g_i}(t) + \omega_{c_i}(t)}. \tag{2.14}$$

This ensures that the tissue percentage at each voxel is compatible with the tissue density maps and that $p_{w_i}(t) + p_{g_i}(t) + p_{c_i}(t) = 1$ for $\forall i \in \Omega_2$.

Let us note that in equation (2.1) the tumour is only subject to displacement, not compression. The reason for this assumption is that gliomas, in contrast to other solid tumours, infiltrate the surrounding tissue, and thus the pressure acting from the tissue on the tumour is minimal. However, if tumour compression is of

interest, this can be achieved by including the convection term (i.e. $-\boldsymbol{u}\nabla\cdot\vec{v}$) on the right-hand side of equation (2.1).

2.1.4. Further considerations

The model can be further updated to account for the anisotropic tumour cell migration along the fibres in the white matter. This can be achieved by replacing the identity matrix $\mathbb{I}$ by a tensor constructed based on the water diffusion tensor obtained through diffusion tensor imaging (DTI), as done in previous works [49,75–78]. Patient-specific DTI scans have the potential to inform the speed and direction of the tumour infiltration in the white matter. There are, however, two reasons why DTI-based infiltration is not considered in our model. First, since DTI measures water diffusion, the DTI signal is corrupted in the oedematous regions owing to increased water content, which can have an adverse effect on the simulated infiltration in the tumour region and its proximity. Second, it is not clear how the orientation of the tissue fibres is affected during tissue compression and deformation caused by the growing tumour. Therefore, in this paper, the tumour infiltration is only constrained by anatomical structures, whereas the deployment of DTI in the presence of the tumour mass effect might require further studies.

Additional model updates can be achieved by including a damping effect in the diffusion term informed by von Mises stress, as presented in [35,79]. This approach accounts for the inhibition in tumour expansion caused by local tissue stress, as observed experimentally for solid tumours [80]. However, in the case of diffusive glioblastomas [81,82] and some other cancers [83,84], experiments suggest increased tumour invasiveness in response to elevated local pressure and compression. More studies are thus required to fully understand the tumour behaviour in relation to its micro-environment and computational models such as [35,79] can assist such studies. In this paper, we consider only tissue-dependent tumour infiltration to keep the number of model parameters minimal.

2.2. Numerical formulation

This section presents how the DDM can be deployed to reduce the computational intensity of the proposed model. Details of the numerical implementation are discussed afterwards.

2.2.1. Diffuse domain formulation

The computational cost of the proposed model is largely determined by the numerical solution of the Helmholtz equations (2.9) and (2.10). Its numerical discretization with the FD method leads to a system of linear equations with a non-symmetric matrix. The non-symmetry is due to the complex brain anatomy and the imposed no-flux boundary condition (equation (2.10)). In turn, many efficient numerical methods such as Jacobi, Gauss–Seidel or conjugate gradient methods cannot be used since they all require symmetric matrices. However, this issue can be efficiently overcome by the DDM [72]. The DDM offers a way to replace a system of equations defined on a complex domain by a new set of equations defined on an arbitrary regular domain with desired boundary conditions. In our case, the Helmholtz equation defined at Ω_2 can be replaced by a new set of equations defined on regular domain Ω_3 with a zero Dirichlet boundary condition on $\partial\Omega_3$, resulting in a system of linear equations with a symmetric matrix. The DDM method uses a so-called phase-field function $\boldsymbol{\psi}:=\{\psi_i\}_{i=1}^{N}\in\Omega_3$ to capture the relationship between the domains Ω_2 and Ω_3. The phase-field function $\boldsymbol{\psi}$ is a smoothed version of the characteristic function $\boldsymbol{\chi}_{|_{\Omega_2}}$ of the domain Ω_2, i.e. $\psi_i=1$ for $i\in\Omega_2$, $\psi_i=0$ for $i\in\Omega_3\backslash\Omega_2$, and ψ varies smoothly at the interface between the domains Ω_2 and Ω_3, such that $\psi(i)=0.5$ for $i\in\partial\Omega_2$, as shown in figure 1. Using the DDM, the Helmholtz equation given by equations (2.9) and (2.10) is reformulated as

$$-\nabla\cdot(\mathcal{M}\cdot\psi\nabla\boldsymbol{p})=\psi\rho\boldsymbol{u}(\mathbf{1}-\boldsymbol{u})-\psi\varkappa\boldsymbol{p}\quad\text{in }\Omega_3,\tag{2.15}$$

$$\boldsymbol{p}=\mathbf{0}\quad\text{on }\partial\Omega_3.\tag{2.16}$$

The FD discretization of the above equations leads to a system of linear equations with a symmetric matrix, thus reducing significantly the numerical complexity of the problem. The phase-field function $\boldsymbol{\psi}$, like Ω_2, does not change over time since it is constrained by a rigid skull. The pressure computed by the above equations in domain Ω_3 can be easily mapped to domain Ω_2 (i.e. brain parenchyma) by multiplication with the characteristic function $\boldsymbol{\chi}_{|_{\Omega_2}}$. The phase-field function can be obtained by solving the Cahn–Hilliard equation [85,86],

$$\frac{\partial\psi}{\partial t}=\nabla\cdot\left(\mathcal{A}(\psi)\cdot\nabla(g'(\psi)-\varepsilon^2\Delta\psi)\right)\in\Omega_3,\tag{2.17}$$

$$\psi(\boldsymbol{t}=\mathbf{0})=\begin{cases}\mathbf{1} & \text{on }\Omega_2,\\ \mathbf{0} & \text{on }\Omega_3\backslash\Omega_2,\end{cases}\tag{2.18}$$

where $g(\boldsymbol{\psi})=\frac{1}{4}\boldsymbol{\psi}^2(1-\boldsymbol{\psi})^2$ is a double-well potential and the term $\mathcal{A}(\boldsymbol{\psi})$ controls the behaviour of the phase-field function at the interface, while ε is the prescribed interface thickness. Taking $\mathcal{A}(\boldsymbol{\psi})=\sqrt{4g(\boldsymbol{\psi})}$ limits interface displacement under the Cahn–Hilliard dynamics. The Cahn–Hilliard equation is solved in time until the phase-field function reaches a smooth interface with the prescribed thickness. The desired width of the interface depends on the application; in this case, the interface width of 3 voxels (i.e. 3 mm) is considered.

Algorithm 1. Implementation of the tumour-induced brain deformation model.

1. *Initialise*: $t=\mathbf{0}$, $\boldsymbol{u}(\boldsymbol{t}=\mathbf{0})=\boldsymbol{u}_0$, $\omega_s(\boldsymbol{t}=\mathbf{0})=\omega_{s_0}$ for $s\in\{w,g,c\}$
2. Compute tissue percentage by equation (2.14)
3. **while** $(t\le T)$ **do**
4. Compute time step $\tau=\min(\tau_1,\tau_2)$, where τ_1 and τ_2 are time steps constrained by the numerical stability of equations (2.1) and (2.11)
5. Compute the **pressure** $\boldsymbol{p}(t)$ by solving equations (2.15) and (2.16)
6. Compute the **deformation field** $\vec{\boldsymbol{v}}(t)$ by solving equations (2.5) and (2.7)
7. Update the **tumour** state by solving equations (2.1) and (2.2)
8. Update the **brain tissue** by solving equations (2.11) and (2.12)
9. Recompute the **tissue percentage** by equation (2.14)
10. $t=t+\tau$
11. **end while**

To simplify the process and to avoid re-computation of the phase-field function for each new patient, affine image registration can be used instead. More specifically, we provide the brain MRI atlas with the binary brain mask (i.e. $\boldsymbol{\chi}_{|_{\Omega_2}}$) and the corresponding phase-field function computed by equation (2.17).[1] For each new patient, the patient-specific phase-field function can be obtained by computing an affine registration, $\mathcal{F}$, that maps the atlas brain mask to the patient's brain mask. The resulting registration $\mathcal{F}$ is then used to map the pre-computed atlas phase-field function to the patient's brain, leading to the patient-specific phase-field function. To ease the process, an automated image-registration software as well as brain atlas are provided.[2,3]

We remark that the DDM approach is used only for the Helmholtz equation. In principle, the whole model could be expressed in the DDM formalism. However, if the simulation domain contains very fine anatomical structures, it might not be possible for the phase-field function to have a smooth interface and preserve the structures at the same time. For instance, the separation between frontal brain lobes often consists of only 1–2 voxels in some regions, and thus a phase-field function with ε of even 1 voxel could distort the separation between the hemispheres, creating artificial pathways for tumour infiltration.

2.2.2. Implementation

A numerical implementation of the proposed model is outlined in algorithm 1, while the software is publicly available.[1] The software uses the FD method for the space discretization together with forward Euler time integration. The Helmholtz equation, given by equations (2.15) and (2.16), is solved with a multigrid preconditioned conjugate gradient method [87] using the *hypre* library [88]. The advection–convection equation (2.11) is solved with the fifth-order weighted essentially non-oscillatory (WENO5) scheme [89]. The advantage of the WENO5 scheme is its capability to achieve highly accurate solutions in smooth regions while maintaining stable, non-oscillatory transitions in regions with sharp discontinuities [90], which appear for instance at interfaces between the CSF and brain tissue. A high-performance implementation is achieved through a hybrid OpenMP and MPI parallelization. For the software and tutorial, please refer to our repository.[1]

3. Results

The proposed model is tested on synthetic and clinical cases. The synthetic case is used to illustrate the model's capability of simulating tumour progression and the corresponding mass effect. The relation between ICP elevation and neurological symptoms is explored. The model is then applied to clinical cases of patients with HGG and LGG lesions. The HGG cases exhibit significant brain deformations; however, owing to the aggressive nature of the disease only scans from a single time point prior to treatment are available. These cases are used to demonstrate the model's capability of reproducing realistic and large brain deformations. Afterwards, data showing tumour progression from LGG to HGG are used to assess the potential of the model to capture disease progression over time. The synthetic case uses healthy brain anatomy obtained from the SRI24 Atlas [91], while the patient cases are obtained from the Brain Tumour Segmentation (BraTS) challenge [92,93].

3.1. Synthetic case

For the synthetic case, brain anatomy from a healthy subject provided by the SRI24 Atlas is used to simulate the disease progression over time. The brain tissue segmentation is provided together with the atlas. The tumour is initialized as a point source in the right frontal lobe and its progression is simulated over a period of 600 days using the following model parameters: $D_w = 1.3 \times 10^{-3}$ (cm^2/day), $D_g = 1.3 \times 10^{-4}$ (cm^2/day), $\rho = 1.2 \times 10^{-2}$ (1/day), $\varkappa_g = 2.0 \times 10^{-3}$ (day/cm^2), $\varkappa_w = 2.0 \times 10^{-2}$ (day/cm^2), $\varkappa_c = 2.0 \times 10^{-1}$ (day/cm^2) and $\mathcal{M} = 8.53 \times 10^{-9}$ (cm$^2 \cdot$ mmHg$^{-1} \cdot$ s^{-1}). The values of parameters (D_w, D_g, ρ) were taken from [31,94] and $\mathcal{M}$ from [74], while values of $\varkappa_w$, $\varkappa_g$, $\varkappa_c$ were chosen empirically.

Figures 2 and 3 show disease progression over time in two- and three-dimensional views. The mass effect of the growing tumour causes brain deformations, including ventricle compression and brain midline displacement, where the latter is more visible in the three-dimensional visualization shown in figure 3. The resulting tumour morphology has a complex pattern compatible with the brain anatomy. The ICP, shown in figure 2*b*, is directly derived from the growing tumour and is constrained by the patient-specific brain anatomy. The model identified the highest pressure accumulation in the frontal lobe, where the growing tumour compresses the brain tissue against the inner wall of the skull. On the other hand, the pressure in the ventricles is much lower, which is consistent with the capability of the CSF to relax the pressure [95]. The deformation field, shown in figure 2*c*, is most dominant at the interface between the tumour and the tissues, i.e. the region where the bulk tumour presses most on the surrounding tissue, while its effect decreases with increasing distance from the tumour. The model predictions can be used to assist clinical interventions, such as ICP management or surgery planning. The distribution of the ICP can be used to estimate the neurological symptoms caused by the increased pressure in the specific brain centres, as shown in figure 2*d*. For instance, in the presented case the pressure elevation in the frontal lobe, as seen in the initial stages of the disease, can affect the subject's behaviour and concentration. As the pressure elevation progresses to the motor cortex, deterioration of motor functions can be expected, followed by impairment of perception caused by further disease progression to the sensory cortex in the parietal lobe. Interestingly, the identified ICP values are also comparable to the pathological values reported in table 1. The latter time points show intracranial hypertension, which is also compatible with the brain midline displacement (shown in figure 3), both representing critical conditions. For clinically relevant predictions, however, model calibration to the patient-specific conditions is needed. This example illustrates the potential of the model to simulate tumour progression, together with the brain deformations and ICP increase over time.

3.2. High-grade glioma cases

To assess the ability of the model to produce realistic brain deformations, the model is used to reproduce the tumour mass effect observed in MRI scans of patients diagnosed with HGG. Figure 4*a*,*b* shows fluid-attenuated inversion recovery (FLAIR) and T1-weighted (T1w) MRI scans of two patients at the time of tumour detection. The FLAIR scan provides good contrast between healthy tissue and tumour (seen as bright enhancement), while the contrast between white and grey matter is less pronounced. On the other hand, the T1w MRI shows lower enhancement in the lesion but superior contrast between the distinct brain tissues. The FLAIR scan is therefore used to detect the tumour extent while the T1w MRI is deployed to estimate the brain anatomy.

To perform the simulation, we would like to initialize the tumour in the patient's tumour-free non-deformed anatomy and model the disease progression over time, until it reaches the state visible on the patient's scans. Since the scans with the patient's healthy anatomy are usually not available, we approximate the initial deformation-free anatomy through

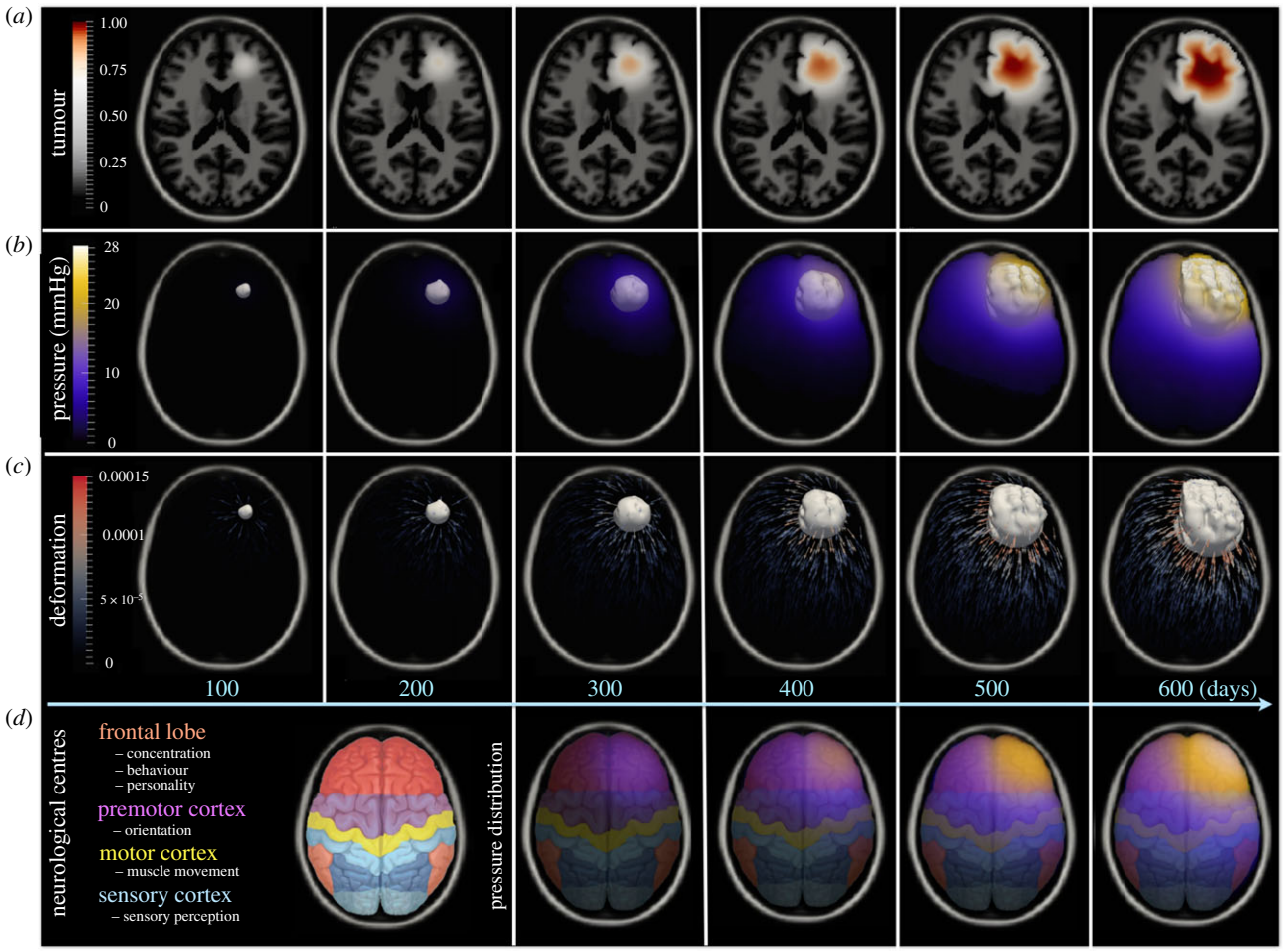

Figure 2. Simulation of disease progression over 600 days in the synthetic case. The subplot (*a*) shows a two-dimensional slice of the brain anatomy with the tumour, while the colour bar indicates the tumour cell density. Tumour progression results in compression of the right ventricle and brain midline displacement in the frontal lobe, the latter one being more visible in figure 3. The pressure distribution and deformation field, together with the tumour outline, shown as the white iso-surface given by $u = 0.3$, are depicted in three dimensions in the subplots (*b*) and (*c*), respectively. The pressure values correspond to the tumour-induced pressure increase over the subject's ICP before the onset of disease. The subplot (*d*) shows neurological brain centres mapped to the patient's anatomy, followed by a visualization of the pressure distribution superimposed on the top of the specific neurological centres. For visualization purposes, the last row shows the pressure distribution from day 300 onwards.

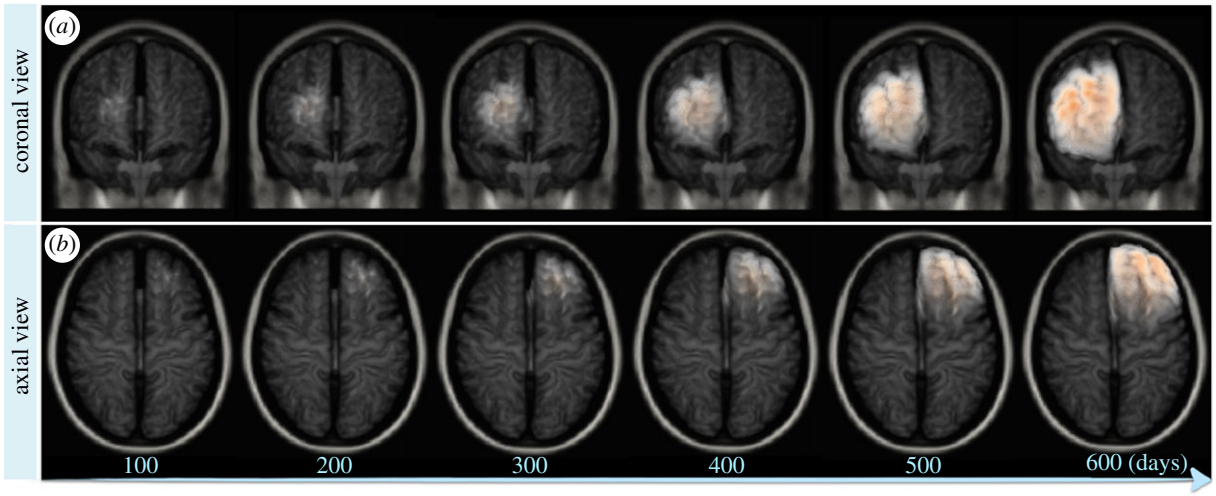

Figure 3. Visualization of the brain midline displacement over time in the synthetic case. The results correspond to the same subject and simulation depicted in figure 2. The three-dimensional visualizations, provided in (*a*) coronal and (*b*) axial view, show brain midline shift, which is one of the indicators of critical conditions. For visualization purposes, the CSF is not depicted.

image registration. More specifically, the T1w MRI scan from the SRI24 atlas [91] is mapped to the patient's T1w scan using affine ANTs [96] registration.[3] The approximated healthy anatomies of both patients are shown in figure 4*c*. This approach provides a reasonable approximation of the deformation-free anatomy in most cases. However, the affine

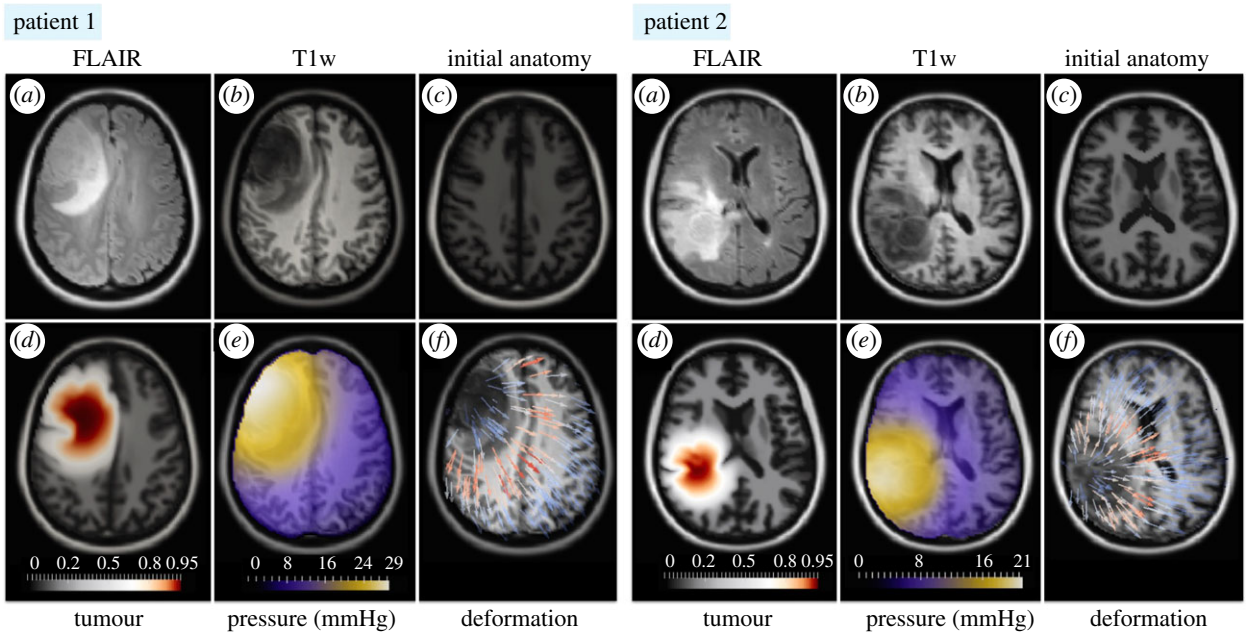

Figure 4. Simulation of disease progression in two patients with HGG. The subplots (*a*,*b*) show FLAIR and T1w MRI scans of each patient from the time of the tumour detection. Since the scans with patient brain anatomy before the onset of the disease are not available, affine registration of the brain atlas to the patients' preoperative MRI scans is used to approximate the tumour-free brain anatomy. The resulting tumour-free brain anatomy is shown in subplots (*c*) and serves as the initial condition for the simulation. The tumour is initialized as a point source in the centre of mass of the FLAIR-enhancing lesion and its progression is simulated over time until it reaches a mass comparable to the tumour visible on the patients' scans. Subplot (*d*) shows the simulated tumour and its effect on the surrounding brain tissue. The colour bar indicates the tumour cell density. The subplots (*e*,*f*) show the simulated pressure distribution and the deformation field overlaid on the patients' T1w MRI scans. The predicted brain deformations mimic the state of the disease visible in the patients' MRI scans. For each patient, the slice across the tumour centre of mass is shown.

registration might not be sufficient to capture atypical anatomical morphologies, such as enlarged ventricles, which might require manual correction. In the simulation, the tumour is initialized as a point source at the centre of mass of the FLAIR-enhancing lesion. The time of the tumour growth, from its onset to detection, is not known in practice. However, from the simulation perspective, one can obtain the same tumour morphology with different combinations of time-dependent parameters, such as T and speed of growth, i.e. (D_w, ρ), as shown in [31,73]. Since the aim of these examples is to illustrate the potential of the model to generate realistic brain deformations, the same parameters as in the synthetic case are used; except the final time T, which is chosen manually by comparing the extent of the real and the predicted tumour.

The results of the model simulations for both cases are shown in figure 4*d–f*. The predicted tumour mass effect is in good qualitative agreement with the tumour-induced deformations observed in the patients' MRI scans. In the case of patient 1, the model correctly predicts the midline displacement, while for patient 2 it accurately reproduces the compression of the ventricles. The simulated tumours have complex morphology similar to tumour patterns seen in the patients' scans. Figure 4*e* shows the predicted ICP distribution overlaid on the patients' T1w MRI scans. The estimated pressure distribution closely follows the morphology of the visible tumour, with the highest pressure accumulation mainly in the tumour core close to the skull. The high ICP values imply intracranial hypertension in both patients (table 1), which is a reasonable estimate given the large size of the lesions. The deformation field, shown in figure 4*f*, is most pronounced at the outlines of the visible tumour, i.e. the regions where the bulk tumour presses most on the surrounding tissue. Small deviations can be attributed to the discrepancies in the approximation of the initial tumour-free brain anatomy. For instance, the ventricles in the frontal lobe of patient 2 appear smaller in the approximated initial anatomy than in the patient's scans. These examples demonstrate the feasibility of the model to reproduce a realistic tumour mass effect, even in the presence of large deformations.

3.3. Low-grade glioma case

We test the feasibility of the model to capture the disease progression over time in a patient case with MRI scans from two different time points. Figure 5*a*,*b*,*f*,*g* shows the patient's scans, where the first time point T_1 corresponds to an LGG lesion from the time of disease detection, while the second time point T_2 shows the tumour transition to HGG. We note that the glioma scans, showing tumour progression over multiple time points, are relatively rare since patients usually undergo treatment or tumour resection. Since in this case data from two time points are available, the scan from the first time point T_1 could be used to initialize the simulation, both the tumour cell density and the brain anatomy, and the model would simulate the disease progression to the second time point T_2. This approach, however, poses a few challenges. First, the patient's brain anatomy below the visible tumour is not known. Second, since the MRI scan captures only the tumour morphology, the tumour cell density and the tumour infiltration beyond the visible tumour borders are unknown. Such uncertainties in the initial condition would significantly affect the model prediction. Moreover, since these scans come from a public database focused on tumour segmentation, the acquisition time of the scans is

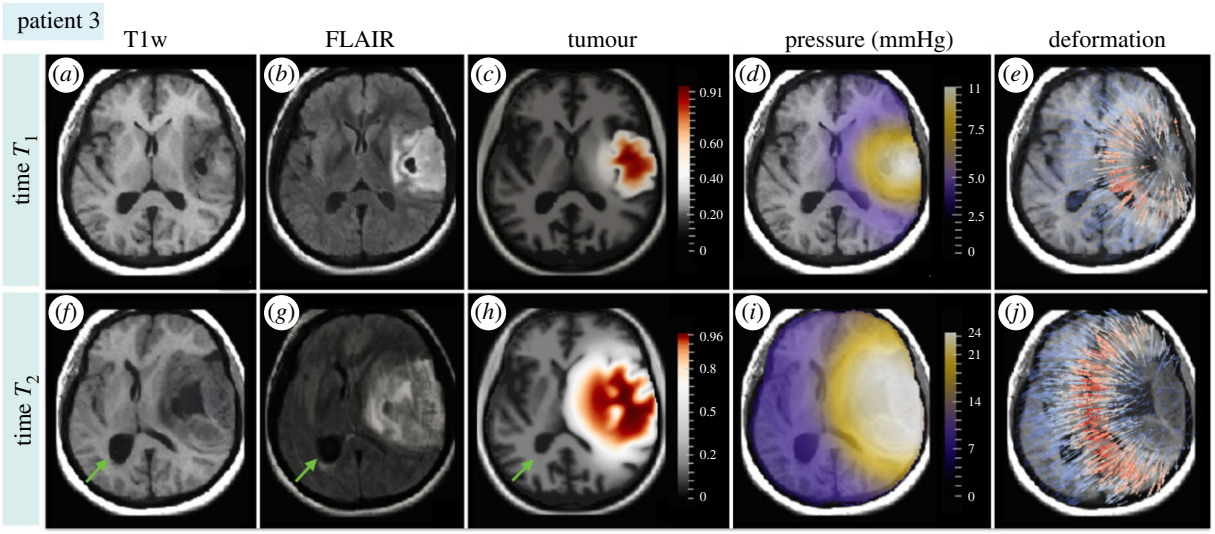

Figure 5. Simulation of disease progression over time. Subplots (*a*,*b*) and (*f*,*g*) show the patient's T1w and FLAIR MRI scans acquired at two different time points, T_1 (the first row) and T_2 (the second row). The first time point shows LGG at the time of the tumour detection, while the second time point depicts the tumour progression to HGG. For the simulation, the tumour is initialized as a point source in the deformation-free anatomy, similarly to the previous cases, and its progression is simulated from the time of disease onset (i.e. $t = 0$ (days)) through time $t = T_1$ to time $t = T_2$. The specific values for parameters T_1 and T_2 are found manually by comparing the mass of the simulated and the patient's tumour visible on the scans. Results of the simulation at $T_1 = 200$ (days) and $T_2 = 700$ (days) are depicted in (*c*–*e*) and (*h*–*j*), respectively. Subplots (*c* and *h*) show the simulated tumour and its effect on the surrounding anatomy for each corresponding time point. The colour bars indicate the tumour cell density. The model correctly predicts a small mass effect at time T_1, while at time T_2 it correctly captures the compression of the right ventricle and the midline shift. However, the model did not capture the enlargement of the left ventricle at time T_2 (marked by green arrows), which stems from the changes in CSF circulation. Subplots (*d*,*e*) and (*i*,*j*) show the predicted pressure distribution and the deformation field visualized on top of the patient's T1w MRI scans from the corresponding time points. At time T_1, the model predicts mild hypertension, which is compatible with low-grade tumours, while more advanced hypertension is estimated as the tumour progresses to an HGG at time T_2. The deformation field is most prominent at the borders of the visible tumour, i.e. the region where the bulk tumour presses most on the surrounding tissue, indicating the deformations towards the brain midline. This example demonstrates that, except for the changes in the CSF circulation, the model can capture disease progression over time.

not provided. But even if the time span between the two time points were known, the disease most likely does not proceed at a constant pace owing to treatment. Since the aim of this example is to assess the ability of the model to capture tumour progression over time, rather than provide patient-specific predictions, a similar strategy as in the previous cases is applied. In particular, the tumour is initialized as a point source in the deformation-free anatomy and this time point is considered as the initial time $t = 0$ (days). The initial brain anatomy is obtained by mapping the brain atlas to the patient's T1w scan from the first time point, i.e. T_1. The initial tumour location is chosen as the centre of mass of the tumour visible on the FLAIR scan from time T_1. The tumour progression is simulated from the time of disease onset, i.e. $t = 0$ (days), through the time of the tumour detection at $t = T_1$ (days) until the final time $t = T_2$ (days) using the same parameter values as in the previous cases. The time points corresponding to the patient's scans were found manually by comparing the extent of the simulated and real tumour, and were estimated as $T_1 = 200$ (days) and $T_2 = 700$ (days). The additional benefit of this approach is that the model predictions can be evaluated at two different time points instead of one.

The results of the simulation at time points T_1 and T_2 are shown in figure 5. The model accurately predicts a small tumour mass effect at the first time point, which is consistent with the LGG visible on the patient's first scan. The estimated pressure distribution and the deformation field follow the morphology of the actual tumour. The moderate elevation in the ICP implies the onset of intracranial hypertension (table 1). At the second time point, the model correctly captures the disease progression, including the compression of the right ventricle and the brain midline shift. The increased ICP indicates advanced intracranial hypertension, typical for HGG, with a high-pressure accumulation in the whole tumour core. However, the model did not capture the enlargement of the left ventricle in the second time point, marked by the green arrows in figure 5. Such ventricular enlargement happens in some patients owing to changes in CSF circulation, which can be caused either by the tumour itself or as a response to treatment [97]. Since the model does not account for the CSF circulation such deformations are not captured. This example shows that, except for ventricular enlargement, the model can provide realistic predictions about disease progression over time. Such predictions can serve as the worst-case scenario estimates about disease progression in the absence or insufficiency of treatment.

4. Conclusion

This paper proposes a novel model coupling glioma progression, tumour mass effect and ICP dynamics. Synthetic and clinical cases are used to illustrate the model's capability to capture realistic disease progression and brain deformations and to estimate the ICP distributions. The main advantage of the proposed approach is that the ICP is directly derived from the tumour dynamics and the patient-specific anatomy. This allows for estimates of critical conditions such as hypertension, brain midline shift or neurological

impairments caused by high-pressure accumulation in specific brain areas. The distribution of ICP has further potential to guide surgical interventions.

The model could also be used to guide deformable image registration of patients' brain scans from different time points. Another interesting application would be to deploy the model towards the discovery of novel prognostic markers. In particular, markers such as midline shift [9,98] or lateral ventricle displacement [99] are often used as indirect measures of mass effect and they show a strong correlation with survival. These markers, however, measure only a displacement of a single point. On the other hand, the model captures the full deformation field in a three-dimensional context. In this way, the displacement of multiple brain landmarks can be quantified and correlated with the patient survival/prognosis, potentially revealing new predictive markers.

A limitation of the proposed model is that it does not account for the circulation of CSF within and outside of the brain. As a consequence, the model cannot capture swelling of the ventricles, which can happen in some patients owing to the presence of the tumour or as a response to the treatment. Future works should thus account for the role of CSF circulation and its effect on ventricular deformations. Of particular interest would also be model extension accounting for distortion of the brainstem, caused either by CSF occlusion along the brainstem or by tumour infiltration into the brainstem itself, which have been recently identified as characteristic features presented in final-stage glioblastoma patients [100].

In the future the model can also be extended by incorporating various factors such as anisotropic tumour infiltration informed by patient-specific DTI [49,78,101], stress-constrained tumour invasion [79], the Allee effect [102] or go-or-grow principle [103,104]. Another compelling direction is to model gross tumour resection and consequent changes. The resection can be modelled by removing the tumour and the resection path (i.e. the tissue leading from the skull to the tumour) and by replacing the void with CSF. The resection cavity can be estimated from the postoperative scans. The presented model can then be used to simulate the progression and mass effect of the residual tumour in the absence of treatment, including tumour-induced compression of the resection cavity. However, the postoperative brain anatomy undergoes significant tumour-unrelated changes such as tissue decompression, which are not captured by the current model. The model only considers the tumour-induced pressure and mass effect. Once the tumour is resected, the pressure source is removed and the tumour-induced pressure drops to zero, i.e. to the patient's normal ICP. Although this is compatible with the outcome of surgery, the uniform pressure in the model does not generate the deformation force to drive the tissue decompression. This could be overcome by including a sink term for the pressure inside the resection cavity to drive the tissue relaxation. The relaxation of residual stresses can also drive tissue decompression (e.g. [10,105–109]). Further studies are however required to understand and correctly capture postoperative brain biomechanical changes.

To facilitate model calibration from patient data, the proposed model relies on a small number of parameters. The model calibration and accuracy of patient-specific predictions should be tested on a larger patient cohort in the following studies. The work presented here serves as a proof of concept that the proposed model holds the potential to capture glioma progression and accompanying tissue deformations and pressure dynamics in the patient's brain. These results encourage future studies of patient-specific model predictions aiming to assist clinical interventions by providing non-invasive estimates about the patient's state and the disease progression over time. Finally, to facilitate deployment of the proposed methodology, a highly parallel implementation of the model is publicly released.

Ethics. The patients' medical scans come from a publicly available database provided by the BraTS challenge [92,93].

Data accessibility. All code used in this work is publicly available in https://github.com/JanaLipkova as the following repositories: *GliomaSolver*—the model and tutorial;[1] *Registration*—image registration;[2] and *S3*—tissue segmentation tool.[3]

Authors' contributions. J.L.: conceptualization, data curation, formal analysis, investigation, methodology, resources, software, validation, visualization, writing—original draft; B.M.: conceptualization, project administration, resources, supervision, writing—original draft; B.W.: resources, supervision, writing—original draft; P.K.: resources, supervision; J.S.L.: conceptualization, funding acquisition, investigation, methodology, project administration, supervision, writing—original draft. All authors gave final approval for publication and agreed to be held accountable for the work performed herein.

Competing interests. We declare we have no competing interests.

Funding. J.S.L. acknowledges partial support from the NSF through grant nos. DMS-1953410 and DMS-1763272 and the Simons Foundation (594598QN) for an NSF-Simons Center for Multiscale Cell Fate Research. B.M. acknowledges support through the Helmut-Horten-Foundation. J.S.L. also thanks the National Institutes of Health for partial support through grant no. 1U54CA217378-01A1 for a National Center in Cancer Systems Biology at UC Irvine and grant no. P30CA062203 for the Chao Family Comprehensive Cancer Center at UC Irvine.

Endnotes

[1]https://github.com/JanaLipkova/GliomaSolver.
[2]Tissue segmentation software: https://github.com/JanaLipkova/s3.
[3]Automated image-registration tool: https://github.com/JanaLipkova/Registration.

References

1. Stupp R *et al.* 2005 Radiotherapy plus concomitant and adjuvant temozolomide for glioblastoma. *N. Engl. J. Med.* **352**, 987–996. (doi:10.1056/NEJMoa043330)
2. Kramer DB. 2013 Survival in patients with glioblastoma receiving valganciclovir. *N. Engl. J. Med.* **368**, 2049–2052. (doi:10.1056/NEJMp1302723)
3. Stupp R, Brada M, Van Den Bent MJ, Tonn JC, Pentheroudakis GE. 2014 High-grade glioma: ESMO Clinical Practice Guidelines for diagnosis, treatment and follow-up. *Ann. Oncol.* **25**(Suppl_3), iii93–iii101. (doi:10.1093/annonc/mdu050)
4. Claus EB *et al.* 2015 Survival and low-grade glioma: the emergence of genetic information. *Neurosurg. Focus* **38**, E6. (doi:10.3171/2014.10.FOCUS12367)

5. Sizoo EM, Braam L, Postma TJ, Pasman HR, Heimans JJ, Klein M, Reijneveld JC, Taphoorn MJ. 2010 Symptoms and problems in the end-of-life phase of high-grade glioma patients. *Neuro Oncol.* **12**, 1162–1166. (doi:10.1093/neuonc/nop045)
6. Sizoo EM *et al.* 2013 The end-of-life phase of high-grade glioma patients: a systematic review. *Support. Care Cancer* **22**, 847–857. (doi:10.1007/s00520-013-2088-9)
7. Pace A *et al.* 2017 European Association for Neuro-Oncology (EANO) guidelines for palliative care in adults with glioma. *Lancet Oncol.* **18**, e330–e340. (doi:10.1016/S1470-2045(17)30345-5)
8. Giammalva GR, Iacopino DG, Azzarello G, Gaggiotti C, Graziano F, Gulì C, Pino MA, Maugeri R. 2018 End-of-life care in high-grade glioma patients. The palliative and supportive perspective. *Brain Sci.* **8**, 125. (doi:10.3390/brainsci8070125)
9. Gamburg ES, Regine WF, Patchell RA, Strottmann JM, Mohiuddin M, Young AB. 2000 The prognostic significance of midline shift at presentation on survival in patients with glioblastoma multiforme. *Int. J. Rad. Oncol. Biol. Phys.* **48**, 1359–1362. (doi:10.1016/S0360-3016(00)01410-3)
10. Jain RK, Martin JD, Stylianopoulos T. 2014 The role of mechanical forces in tumor growth and therapy. *Annu. Rev. Biomed. Eng.* **16**, 321–346. (doi:10.1146/annurev-bioeng-071813-105259)
11. Harpold HLP, Ellsworth KRS, Alvord C. 2007 The evolution of mathematical modeling of glioma proliferation and invasion. *J. Neuropathol. Exp. Neurol.* **66**, 1–9. (doi:10.1097/nen.0b013e31802d9000)
12. Alfonso JC, Talkenberger K, Seifert M, Klink B, Hawkins-Daarud A, Swanson KR, Hatzikirou H, Deutsch A. 2017 The biology and mathematical modelling of glioma invasion: a review. *J. R. Soc. Interface* **14**, 20170490. (doi:10.1098/rsif.2017.0490)
13. Jackson PR, Juliano J, Hawkins-Daarud A, Rockne RC, Swanson KR. 2015 Patient-specific mathematical neuro-oncology: using a simple proliferation and invasion tumor model to inform clinical practice. *Bull. Math. Biol.* **77**, 846–856. (doi:10.1007/s11538-015-0067-7)
14. Swan A, Hillen T, Bowman JC, Murtha AD. 2018 A patient-specific anisotropic diffusion model for brain tumour spread. *Bull. Math. Biol.* **80**, 1259–1291. (doi:10.1007/s11538-017-0271-8)
15. Cristini V, Lowengrub J. 2010 *Multiscale modeling of cancer*. Cambridge, UK: Cambridge University Press.
16. Yan H, Romero-López M, Benitez LI, Di K, Frieboes HB, Hughes CC, Bota DA, Lowengrub JS. 2017 3D mathematical modeling of glioblastoma suggests that transdifferentiated vascular endothelial cells mediate resistance to current standard-of-care therapy. *Cancer Res.* **77**, 4171–4184. (doi:10.1158/0008-5472.CAN-16-3094)
17. Ezhov I, Lipkova J, Shit S, Kofler F, Collomb N, Lemasson B, Barbier E, Menze B. 2019 Neural parameters estimation for brain tumor growth modeling. In *Int. Conf. on Medical Image Computing and Computer-Assisted Intervention*, *Shenzhen, China*, *13–17 October 2019*, pp. 787–795. Berlin, Germany: Springer.
18. Mang A, Bakas S, Subramanian S, Davatzikos C, Biros G. 2020 Integrated biophysical modeling and image analysis: application to neuro-oncology. *Annu. Rev. Biomed. Eng.* **22**, 309–341. (doi:10.1146/annurev-bioeng-062117-121105)
19. Yankeelov TE, Atuegwu N, Hormuth D, Weis JA, Barnes SL, Miga MI, Rericha EC, Quaranta V. 2013 Clinically relevant modeling of tumor growth and treatment response. *Sci. Transl. Med.* **5**, 187ps9–187ps9. (doi:10.1126/scitranslmed.3005686)
20. Angelini ED, Clatz O, Mandonnet E, Konukoglu E, Capelle L, Duffau H. 2007 Glioma dynamics and computational models: a review of segmentation, registration, and in silico growth algorithms and their clinical applications. *Curr. Med. Imag.* **3**, 262–276. (doi:10.2174/157340507782446241)
21. Bruno R *et al.* 2020 Progress and opportunities to advance clinical cancer therapeutics using tumor dynamic models. *Clin. Cancer Res.* **26**, 1787–1795. (doi:10.1158/1078-0432.CCR-19-0287)
22. Rockne RC *et al.* 2019 The 2019 mathematical oncology roadmap. *Phys. Biol.* **16**, 041005. (doi:10.1088/1478-3975/ab1a09)
23. Alfonso JC, Talkenberger K, Seifert M, Klink B, Hawkins-Daarud A, Swanson KR, Hatzikirou H, Deutsch A. 2017 The biology and mathematical modelling of glioma invasion: a review. *J. R. Soc. Interface* **14**, 20170490. (doi:10.1098/rsif.2017.0490)
24. Unkelbach J, Menze BH, Konukoglu E, Dittmann F, Le M, Ayache N, Shih HA. 2014 Radiotherapy planning for glioblastoma based on a tumor growth model: improving target volume delineation. *Phys. Med. Biol.* **59**, 747. (doi:10.1088/0031-9155/59/3/747)
25. Liu J, Hormuth DA, Davis T, Yang J, McKenna MT, Jarrett AM, Enderling H, Brock A, Yankeelov TE. 2021 A time-resolved experimental–mathematical model for predicting the response of glioma cells to single-dose radiation therapy. *Integr. Biol.* **13**, 167–183. (doi:10.1093/intbio/zyab010)
26. Khajanchi S. 2019 Stability analysis of a mathematical model for glioma-immune interaction under optimal therapy. *Int. J. Nonlinear Sci. Numer. Simul.* **20**, 269–285. (doi:10.1515/ijnsns-2017-0206)
27. Bogdańska MU, Bodnar M, Piotrowska MJ, Murek M, Schucht P, Beck J, Martínez-González A, Pérez-García VM. 2017 A mathematical model describes the malignant transformation of low grade gliomas: prognostic implications. *PLoS ONE* **12**, e0179999.
28. Meghdadi N, Soltani M, Niroomand-Oscuii H, Ghalichi F. 2016 Image based modeling of tumor growth. *Australas. Phys. Eng. Sci. Med.* **39**, 601–613. (doi:10.1007/s13246-016-0475-5)
29. Engwer C, Hillen T, Knappitsch M, Surulescu C. 2015 Glioma follow white matter tracts: a multiscale DTI-based model. *J. Math. Biol.* **71**, 551–582. (doi:10.1007/s00285-014-0822-7)
30. Massey SC *et al.* 2020 Image-based metric of invasiveness predicts response to adjuvant temozolomide for primary glioblastoma. *PLoS ONE* **15**, e0230492. (doi:10.1371/journal.pone.0230492)
31. Lipková J *et al.* 2019 Personalized radiotherapy design for glioblastoma: integrating mathematical tumor models, multimodal scans and Bayesian inference. *IEEE Trans. Med. Imaging* **15**, e0230492.
32. Ezhov I *et al.* 2020 Geometry-aware neural solver for fast Bayesian calibration of brain tumor models. (http://arxiv.org/abs/200904240)
33. Subramanian S, Scheufele K, Mehl M, Biros G. 2020 Where did the tumor start? An inverse solver with sparse localization for tumor growth models. *Inverse Prob.* **36**, 045006. (doi:10.1088/1361-6420/ab649c)
34. Gholami A, Mang A, Biros G. 2014 Image-driven parameter estimation for low grade gliomas. (http://arxiv.org/abs/14086221)
35. Hormuth DA, Al Feghali KA, Elliott AM, Yankeelov TE, Chung C. 2021 Image-based personalization of computational models for predicting response of high-grade glioma to chemoradiation. *Sci. Rep.* **11**, 1–14. (doi:10.1038/s41598-021-87887-4)
36. Konukoglu E, Clatz O, Menze BH, Stieltjes B, Weber MA, Mandonnet E, Delingette H, Ayache N. 2009 Image guided personalization of reaction-diffusion type tumor growth models using modified anisotropic eikonal equations. *IEEE Trans. Med. Imaging* **29**, 77–95. (doi:10.1109/TMI.2009.2026413)
37. Hawkins-Daarud A, Johnston SK, Swanson KR. 2019 Quantifying uncertainty and robustness in a biomathematical model-based patient-specific response metric for glioblastoma. *JCO Clin. Cancer Inform.* **3**, 1–8. (doi:10.1200/CCI.18.00066)
38. Ezhov I *et al.* 2021 Learn-Morph-Infer: a new way of solving the inverse problem for brain tumor modeling. (http://arxiv.org/abs/211104090)
39. Wittek A, Miller K, Kikinis R, Warfield SK. 2007 Patient-specific model of brain deformation: application to medical image registration. *J. Biomech.* **40**, 919–929. (doi:10.1016/j.jbiomech.2006.02.021)
40. Miga MI, Paulsen KD, Hoopes PJ, Kennedy FE, Hartov A, Roberts DW. 2000 In vivo quantification of a homogeneous brain deformation model for updating preoperative images during surgery. *IEEE Trans. Biomed. Eng.* **47**, 266–273. (doi:10.1109/10.821778)
41. Luo M, Larson PS, Martin AJ, Miga MI. 2020 Accounting for deformation in deep brain stimulation surgery with models: comparison to interventional magnetic resonance imaging. *IEEE Trans. Biomed. Eng.* **67**, 2934–2944. (doi:10.1109/TBME.2020.2974102)
42. Hou W, Liu PX, Zheng M, Liu S. 2019 A new deformation model of brain tissues for neurosurgical simulation. *IEEE Trans. Instrum. Meas.* **69**, 1251–1258. (doi:10.1109/TIM.2019.2909247)
43. Miller K, Chinzei K, Orssengo G, Bednarz P. 2000 Mechanical properties of brain tissue *in-vivo*: experiment and computer simulation. *J. Biomech.* **33**, 1369–1376. (doi:10.1016/S0021-9290(00)00120-2)
44. Laksari K *et al.* 2020 Multi-directional dynamic model for traumatic brain injury detection.

J. Neurotrauma **37**, 982–993. (doi:10.1089/neu.2018.6340)

45. Li X, Zhou Z, Kleiven S. 2021 An anatomically detailed and personalizable head injury model: significance of brain and white matter tract morphological variability on strain. *Biomech. Model. Mechanobiol.* **20**, 403–431. (doi:10.1007/s10237-020-01391-8)
46. Wang F, Han Y, Wang B, Peng Q, Huang X, Miller K, Wittek A. 2018 Prediction of brain deformations and risk of traumatic brain injury due to closed-head impact: quantitative analysis of the effects of boundary conditions and brain tissue constitutive model. *Biomech. Model. Mechanobiol.* **17**, 1165–1185. (doi:10.1007/s10237-018-1021-z)
47. Mohamed A, Davatzikos C. 2005 Finite element modeling of brain tumor mass-effect from 3D medical images. In *Int. Conf. on Medical Image Computing and Computer-Assisted Intervention*, *Palm Springs, CA, 26–29 October 2005*, pp. 400–408. Berlin, Germany: Springer.
48. Hogea C, Abraham F, Biros G, Davatzikos C. 2006 A framework for soft tissue simulations with applications to modeling brain tumor mass-effect in 3-D images. *Comput. Biomech. Med.* **52**, 24.
49. Clatz O, Sermesant M, Bondiau PY, Delingette H, Warfield SK, Malandain G, Ayache N. 2005 Realistic simulation of the 3-D growth of brain tumors in MR images coupling diffusion with biomechanical deformation. *Med. Imag. IEEE Trans.* **24**, 1334–1346. (doi:10.1109/TMI.2005.857217)
50. Abler D, Büchler P, Rockne RC. 2019 Towards model-based characterization of biomechanical tumor growth phenotypes. In *Int. Symp. on Mathematical and Computational Oncology*, *Lake Tahoe, NV, 14–15 October 2019,* pp. 75–86. Berlin, Germany: Springer.
51. Hogea C, Biros G, Davatzikos C. 2007 A robust framework for soft tissue simulations with application to modeling brain tumor mass effect in 3D MR images. *Phys. Med. Biol.* **52**, 6893–6908. (doi:10.1088/0031-9155/52/23/008)
52. Hogea C, Davatzikos C, Biros G. 2007 Modeling glioma growth and mass effect in 3D MR images of the brain. In *Int. Conf. on Medical Image Computing and Computer-Assisted Intervention*, *Brisbane, Australia*, *29 October–2 November 2007*, pp. 642–650. Berlin, Germany: Springer.
53. Zacharaki EI, Hogea CS, Shen D, Biros G, Davatzikos C. 2009 Non-diffeomorphic registration of brain tumor images by simulating tissue loss and tumor growth. *Neuroimage* **46**, 762–774. (doi:10.1016/j.neuroimage.2009.01.051)
54. Tunc B, Hormuth D, Biros G, Yankeelov TE. 2021 Modeling of glioma growth with mass effect by longitudinal magnetic resonance imaging. *IEEE Trans. Biomed. Eng.* **68**, 3713–3724. (doi:10.1109/TBME.2021.3085523)
55. Subramanian S, Scheufele K, Himthani N, Biros G. 2020 Multiatlas calibration of biophysical brain tumor growth models with mass effect. In *Int. Conf. on Medical Image Computing and Computer-Assisted Intervention*, *Lima, Peru, 4–8 October 2020*, pp. 551–560. Berlin, Germany: Springer.
56. Uzunova H, Ehrhardt J, Handels H. 2020 Generation of annotated brain tumor MRIs with tumor-induced tissue deformations for training and assessment of neural networks. In *Int. Conf. on Medical Image Computing and Computer-Assisted Intervention*, *Lima, Peru*, *4–8 October 2020*, pp. 501–511. Berlin, Germany: Springer.
57. Subramanian S, Gholami A, Biros G. 2019 Simulation of glioblastoma growth using a 3D multispecies tumor model with mass effect. *J. Math. Biol.* **79**, 941–967. (doi:10.1007/s00285-019-01383-y)
58. Weickenmeier J, Kurt M, Ozkaya E, de Rooij R, Ovaert TC, Ehman RL, Pauly KB, Kuhl E. 2018 Brain stiffens post mortem. *J. Mech. Behav. Biomed. Mater.* **84**, 88–98. (doi:10.1016/j.jmbbm.2018.04.009)
59. Rangel-Castillo L, Gopinath S, Robertson CS. 2008 Management of intracranial hypertension. *Neurol. Clin.* **26**, 521–541. (doi:10.1016/j.ncl.2008.02.003)
60. Singh V, Cheng R. 2021 Neurovascular physiology and neurocritical care. In *Handbook of clinical neurology*, vol. 176 (eds SW Hetts, DL Cooke), pp. 71–80. Amsterdam, The Netherlands: Elsevier.
61. Ghajar J. 2000 Traumatic brain injury. *Lancet* **356**, 923–929. (doi:10.1016/S0140-6736(00)02689-1)
62. Nourallah B, Zeiler FA, Calviello L, Smielewski P, Czosnyka M, Menon DK. 2018 Critical thresholds for intracranial pressure vary over time in non-craniectomised traumatic brain injury patients. *Acta Neurochir. (Wien)* **160**, 1315–1324. (doi:10.1007/s00701-018-3555-3)
63. Balestreri M, Czosnyka M, Hutchinson P, Steiner LA, Hiler M, Smielewski P, Pickard JD. 2006 Impact of intracranial pressure and cerebral perfusion pressure on severe disability and mortality after head injury. *Neurocrit. Care* **4**, 8–13. (doi:10.1385/NCC:4:1:008)
64. Roth C, Ferbert A, Matthaei J, Kaestner S, Engel H, Gehling M. 2019 Progress of intracranial pressure and cerebral perfusion pressure in patients during the development of brain death. *J. Neurol. Sci.* **398**, 171–175. (doi:10.1016/j.jns.2019.01.048)
65. Young JS, Blow O, Turrentine F, Claridge JA, Schulman A. 2003 Is there an upper limit of intracranial pressure in patients with severe head injury if cerebral perfusion pressure is maintained? *Neurosurg. Focus* **15**, 1–7. (doi:10.3171/foc.2003.15.6.2)
66. Cederberg D, Marklund N, Redebrandt HN. 2020 Extreme intracranial pressure elevation >90 mmHg in an awake patient with primary CNS lymphoma–case report. *Acta Neurochir. (Wien)* **162**, 1819–1823. (doi:10.1007/s00701-020-04231-x)
67. Treggiari MM, Schutz N, Yanez ND, Romand JA. 2007 Role of intracranial pressure values and patterns in predicting outcome in traumatic brain injury: a systematic review. *Neurocrit. Care* **6**, 104–112. (doi:10.1007/s12028-007-0012-1)
68. Sadoughi A, Rybinnik I, Cohen R. 2013 Measurement and management of increased intracranial pressure. *Open Crit. Care Med. J.* **6**, 56–65. (doi:10.2174/1874828701306010056)
69. Motuel J, Biette I, Srairi M, Mrozek S, Kurrek MM, Chaynes P, Cognard C, Fourcade O, Geeraerts T. 2014 Assessment of brain midline shift using sonography in neurosurgical ICU patients. *Crit. Care* **18**, 1–8. (doi:10.1186/s13054-014-0676-9)
70. Tu PH, Liu ZH, Chuang CC, Yang TC, Wu CT, Lee ST. 2012 Postoperative midline shift as secondary screening for the long-term outcomes of surgical decompression of malignant middle cerebral artery infarcts. *J. Clin. Neurosci.* **19**, 661–664. (doi:10.1016/j.jocn.2011.07.045)
71. Ellenbogen RG, Sekhar LN, Kitchen N. 2017 *Principles of neurological surgery e-book*. Elsevier Health Sciences.
72. Li X, Lowengrub J, Rätz A, Voigt A. 2009 Solving PDEs in complex geometries: a diffuse domain approach. *Commun. Math. Sci.* **7**, 81. (doi:10.4310/CMS.2009.v7.n1.a4)
73. Menze BH, Leemput KV, Honkela A, Konukoglu E, Weber MA, Ayache N, Golland P. 2011 A generative approach for image-based modeling of tumor growth. In *Information processing in medical imaging* (eds G Székely, HK Hahn). Berlin, Germany: Springer.
74. Swabb EA, Wei J, Gullino PM. 1974 Diffusion and convection in normal and neoplastic tissues. *Cancer Res.* **34**, 2814–2822.
75. Jbabdi S, Mandonnet E, Duffau H, Capelle L, Swanson KR, Pélégrini-Issac M, Guillevin R, Benali H. 2005 Simulation of anisotropic growth of low-grade gliomas using diffusion tensor imaging. *Magn. Reson. Med.* **54**, 616–624. (doi:10.1002/mrm.20625)
76. Cobzas D, Mosayebi P, Murtha A, Jagersand M. 2009 Tumor invasion margin on the Riemannian space of brain fibers. In *Int. Conf. on Medical Image Computing and Computer-Assisted Intervention*, pp. 531–539. Berlin, Germany: Springer.
77. Abler D, Rockne RC, Büchler P. 2019 Evaluating the effect of tissue anisotropy on brain tumor growth using a mechanically coupled reaction–diffusion model. In *New developments on computational methods and imaging in biomechanics and biomedical engineering*, pp. 37–48. Berlin, Germany: Springer.
78. Painter K, Hillen T. 2013 Mathematical modelling of glioma growth: the use of diffusion tensor imaging (DTI) data to predict the anisotropic pathways of cancer invasion. *J. Theor. Biol.* **323**, 25–39. (doi:10.1016/j.jtbi.2013.01.014)
79. Hormuth DA, II SLE, Weis JA, Miga MI, Yankeelov TE. 2018 Mechanically coupled reaction-diffusion model to predict glioma growth: methodological details. *Methods Mol. Biol. (Clifton, NJ)* **1711**, 225.
80. Helmlinger G, Netti PA, Lichtenbeld HC, Melder RJ, Jain RK. 1997 Solid stress inhibits the growth of multicellular tumor spheroids. *Nat. Biotechnol.* **15**, 778–783. (doi:10.1038/nbt0897-778)
81. Kaufman LJ, Brangwynne CP, Kasza KE, Filippidi E, Gordon VD, Deisboeck TS, Weitz DA. 2005 Glioma expansion in collagen I matrices: analyzing collagen concentration-dependent growth and motility

patterns. *Biophys. J.* **89**, 635–650. (doi:10.1529/biophysj.105.061994)

82. Mammoto T, Jiang A, Jiang E, Panigrahy D, Kieran MW, Mammoto A. 2013 Role of collagen matrix in tumor angiogenesis and glioblastoma multiforme progression. *Am. J. Pathol.* **183**, 1293–1305. (doi:10.1016/j.ajpath.2013.06.026)
83. Janet MT, Cheng G, Tyrrell JA, Wilcox-Adelman SA, Boucher Y, Jain RK, Munn LL. 2012 Mechanical compression drives cancer cells toward invasive phenotype. *Proc. Natl Acad. Sci. USA* **109**, 911–916. (doi:10.1073/pnas.1118910109)
84. Sodek KL, Ringuette MJ, Brown TJ. 2009 Compact spheroid formation by ovarian cancer cells is associated with contractile behavior and an invasive phenotype. *Int. J. Cancer* **124**, 2060–2070. (doi:10.1002/ijc.24188)
85. Teigen KE, Li X, Lowengrub J, Wang F, Voigt A. 2009 A diffuse-interface approach for modeling transport, diffusion and adsorption/desorption of material quantities on a deformable interface. *Commun. Math. Sci.* **4**, 1009. (doi:10.4310/CMS.2009.v7.n4.a10)
86. Cahn JW, Hilliard JE. 1958 Free energy of a nonuniform system. I. Interfacial free energy. *J. Chem. Phys.* **28**, 258–267. (doi:10.1063/1.1744102)
87. Gilles L, Vogel CR, Ellerbroek BL. 2002 Multigrid preconditioned conjugate-gradient method for large-scale wave-front reconstruction. *JOSA A* **19**, 1817–1822. (doi:10.1364/JOSAA.19.001817)
88. Falgout RD, Yang UM. 2002 hypre: a library of high performance preconditioners. In *Int. Conf. on Computational Science*, pp. 632–641. Berlin, Germany: Springer.
89. Henrick AK, Aslam TD, Powers JM. 2005 Mapped weighted essentially non-oscillatory schemes: achieving optimal order near critical points. *J. Comput. Phys.* **207**, 542–567. (doi:10.1016/j.jcp.2005.01.023)
90. Lunet T, Lac C, Auguste F, Visentin F, Masson V, Escobar J. 2017 Combination of WENO and explicit Runge–Kutta methods for wind transport in the Meso-NH model. *Mon. Weather Rev.* **145**, 3817–3838. (doi:10.1175/MWR-D-16-0343.1)
91. Rohlfing T, Zahr NM, Sullivan EV, Pfefferbaum A. 2010 The SRI24 multichannel atlas of normal adult human brain structure. *Hum. Brain Mapp.* **31**, 798–819. (doi:10.1002/hbm.20906)
92. Menze BH *et al.* 2014 The multimodal brain tumor image segmentation benchmark (BRATS). *IEEE Trans. Med. Imaging* **34**, 1993–2024. (doi:10.1109/TMI.2014.2377694)
93. Bakas S *et al.* 2018 Identifying the best machine learning algorithms for brain tumor segmentation, progression assessment, and overall survival prediction in the BRATS challenge. (http://arxiv.org/abs/181102629)
94. Harpold HL, Alvord Jr EC, Swanson KR. 2007 The evolution of mathematical modeling of glioma proliferation and invasion. *J. Neuropathol. Exp. Neurol.* **66**, 1–9. (doi:10.1097/nen.0b013e31802d9000)
95. Mokri B. 2001 The Monro–Kellie hypothesis: applications in CSF volume depletion. *Neurology* **56**, 1746–1748. (doi:10.1212/WNL.56.12.1746)
96. Avants BB, Tustison N, Song G. 2009 Advanced normalization tools (ANTS). *Insight J.* **2**, 1–35.
97. Inamasu J, Nakamura Y, Saito R, Kuroshima Y, Mayanagi K, Orii M, Ichikizaki K. 2003 Postoperative communicating hydrocephalus in patients with supratentorial malignant glioma. *Clin. Neurol. Neurosurg.* **106**, 9–15. (doi:10.1016/S0303-8467(03)00060-X)
98. Wach J, Hamed M, Schuss P, Güresir E, Herrlinger U, Vatter H, Schneider M. 2021 Impact of initial midline shift in glioblastoma on survival. *Neurosurg. Rev.* **44**, 1401–1409. (doi:10.1007/s10143-020-01328-w)
99. Steed TC, Treiber JM, Brandel MG, Patel KS, Dale AM, Carter BS, Chen CC. 2018 Quantification of glioblastoma mass effect by lateral ventricle displacement. *Sci. Rep.* **8**, 1–8. (doi:10.1038/s41598-018-21147-w)
100. Drumm MR *et al.* 2020 Extensive brainstem infiltration, not mass effect, is a common feature of end-stage cerebral glioblastomas. *Neuro Oncol.* **22**, 470–479. (doi:10.1093/neuonc/noz216)
101. Metz MC *et al.* 2020 Predicting glioblastoma recurrence from preoperative MR scans using fractional-anisotropy maps with free-water suppression. *Cancers* **12**, 728. (doi:10.3390/cancers12030728)
102. Böttger K, Hatzikirou H, Voss-Böhme A, Cavalcanti-Adam EA, Herrero MA, Deutsch A. 2015 An emerging Allee effect is critical for tumor initiation and persistence. *PLoS Comput. Biol.* **11**, e1004366. (doi:10.1371/journal.pcbi.1004366)
103. Hatzikirou H, Basanta D, Simon M, Schaller K, Deutsch A. 2012 'Go or grow': the key to the emergence of invasion in tumour progression? *Math. Med. Biol.* **29**, 49–65. (doi:10.1093/imammb/dqq011)
104. Pham K, Chauviere A, Hatzikirou H, Li X, Byrne HM, Cristini V, Lowengrub J. 2012 Density-dependent quiescence in glioma invasion: instability in a simple reaction–diffusion model for the migration/proliferation dichotomy. *J. Biol. Dyn.* **6**(Supp. 1), 54–71. (doi:10.1080/17513758.2011.590610)
105. Stylianopoulos T, Martin JD, Snuderi M, Mpekris F, Jain SR, Jain RK. 2013 Co-evolution of solid stress and interstitial fluid pressure in tumors during progression: Implications for vascular collapse. *Cancer Res.* **73**, 3833–3841. (doi:10.1158/0008-5472.CAN-12-4521)
106. Nia HT *et al.* 2016 Solid stress and elastic energy as measures of tumour mechanopathology. *Nat. Biomed. Eng.* **1**, 0004. (doi:10.1038/s41551-016-0004)
107. Stylianopoulos T, Munn LL, Jain RK. 2018 Reengineering the physical microenvironment of tumors to improve drug delivery and efficacy: from mathematical modeling to bench to bedside. *Trends Cancer* **4**, 292–319. (doi:10.1016/j.trecan.2018.02.005)
108. Zhang H, Li B, Shao Y, Feng XQ. 2020 Morphomechanics of tumors. *Curr. Opin. Biomed. Eng.* **15**, 51–58. (doi:10.1016/j.cobme.2020.01.004)
109. Yan H, Ramirez-Guerrero D, Lowengrub J, Wu M. 2021 Stress generation, relaxation and size control in confined tumor growth. *PLoS Comput. Biol.* **17**, e1009701. (doi:10.1371/journal.pcbi.1009701)